

# **Protective coatings on stainless steel bipolar plates for proton exchange membrane (PEM) electrolysers**

A. S. Gago<sup>1,\*</sup>, S. A. Ansar<sup>1</sup>, B. Saruhan<sup>2</sup>, U. Schulz<sup>2</sup>, P. Lettenmeier<sup>1</sup>, N. A. Cañas<sup>1</sup>, P. Gazdzicki<sup>1</sup>, T. Morawietz<sup>3</sup>, R. Hiesgen<sup>3</sup>, J. Arnold<sup>1</sup>, K. A. Friedrich<sup>1,4</sup>

<sup>1</sup>Institute of Engineering Thermodynamics, German Aerospace Centre, Pfaffenwaldring 38-40, 70569, Stuttgart, Germany

<sup>2</sup>Institute of Materials Research, German Aerospace Centre, Linder Hoehe, 51147, Cologne, Germany

<sup>3</sup>University of Applied Sciences Esslingen, Dept. of Basic Science, Kanalstrasse 33, 73728, Esslingen, Germany

<sup>4</sup>Institute for Energy Storage, University of Stuttgart, Keplerstraße 7, 70550, Stuttgart, Germany

---

\*Corresponding author: Tel.: +49 711 6862-8090, fax: +49 711 6862-747, e-mail address: aldo.gago@dlr.de (A. S. Gago).

## Abstract

Proton exchange membrane (PEM) electrolysis is a promising technology for large H<sub>2</sub> production from surplus electricity from renewable sources. However, the electrolyser stack is costly due to the manufacture of bipolar plates (BPPs). Stainless steel can be used as an alternative, but it must be coated. Herein, dense titanium coatings are produced on stainless steel substrates by vacuum plasma spraying (VPS). Further surface modification of the Ti coating with Pt (8 wt% Pt/Ti) deposited by physical vapour deposition (PVD) magnetron sputtering reduces the interfacial contact resistance (ICR). The Ti and Pt/Ti coatings are characterised by scanning electron microscopy (SEM), atomic force microscopy (AFM), X-ray diffraction (XRD), and X-ray photoelectron microscopy (XPS). Subsequently, the coatings are evaluated in simulated and real PEM electrolyser environments, and they managed to fully protect the stainless steel substrate. In contrast, the absence of the thermally sprayed Ti layer between Pt and stainless steel leads to pitting corrosion. The Pt/Ti coating is tested in a PEM electrolyser cell for almost 200 h, exhibiting an average degradation rate of 26.5  $\mu\text{V h}^{-1}$ . The results reported here demonstrate the possibility of using stainless steel as a base material for the stack of a PEM electrolyser.

**Keywords:** PEM electrolysis; cost reduction; stack; bipolar plates; stainless steel; coating

## 1. Introduction

Hydrogen can be used as an energy vector for renewable energies, such as solar or wind, by using water electrolysis systems [1]. Commercially, hydrogen can be electrochemically produced by alkaline and proton exchange membrane (PEM) electrolysis [2], but the investment cost of the latter is currently almost three times higher than that of the former [3]. However, PEM electrolyzers boast the advantages of operating at much higher current densities than the alkaline systems [4]. They also offer a significant opportunity to reduce costs owing to their compact design, but the lifetime of PEM electrolyzers at high performance is still unknown. The key components of PEM electrolyzers that largely determine the cost of the stack are the BPPs [5]. Recently, an EU-funded study reported that 51% of the cost of the stack is attributed to the BPPs, followed by 10% corresponding to the membrane electrode assembly (MEA) manufacture, and only 8% to the precious metal group (PMG) catalysts [6]. Moreover, the stack itself constitutes 60% of the cost of the entire PEM electrolyser system. Therefore, there is an urgent need for low-cost bipolar plates to reduce the cost of PEM electrolysis technology. The high cost of the BPPs is ascribed to the following:

- i) The use of high-purity Ti as the base material for manufacturing the plates [7].
- ii) The complicated and difficult machining process of the flow fields on Ti [8,9].
- iii) The need for coatings on the Ti for reducing the anodisation process [10–13]. The oxide layer that is formed on Ti at high potentials decreases the through-plane electrical conductivity. This layer is detrimental to the performance of unitised regenerative fuel cells (URFCs) operating in electrolysis mode [11,14]. This layer is also expected to have a negative effect on the long-term durability of PEM electrolyzers.

Stainless steel could be used as an alternative, but it must be protected with a highly conductive and corrosion-resistant coating. This metal is cheaper and easier to machine than titanium, but it corrodes when polarised at high overpotentials in an oxidative medium. Moreover, the ions released from the corrosion process poison the MEA of the electrolyser [15,16]. Consequently, a BPP made of stainless steel must be protected with a coating as part of the manufacturing process. This coating should meet the following requirements:

- i) Corrosion resistance at high voltages ( $> 2$  V), in hot ( $T = 65 - 80$  °C) and acidic environments ( $\text{pH} = 0$ ) saturated with  $\text{O}_2$
- ii) High through-plane electrical conductivity and low ICR
- iii) Strong adherence to the substrate, good mechanical properties under compression and minimal differences in the coefficient of thermal expansion within the temperature range of the electrolyser
- iv) Low cost material, and facile and scalable deposition technique. The coating process must be amenable to stacks with large area ( $> 1000$  cm<sup>2</sup>) bipolar plates for use in electrolysers in the megawatt range
- v) Resistance to  $\text{H}_2$  embrittlement if the cathode side will be coated as well.

Requirements (ii), (iii) and (v) are similar to those for coatings for PEM fuel cell (PEMFC) stack stainless steel BPPs [17]. However, requirement (i) is much more difficult to overcome in PEM electrolysers than in fuel cells, as the later operates at lower voltages than the  $\text{H}_2$  generator. Figure 1 shows a scheme of the anode for a PEM electrolyser. The dashed circle indicates the contact area of the coated BPP that is most vulnerable to corrosion in the hostile environment described in (i). Requirement (iv) is aimed at compact PEM electrolysers in the megawatt range, such as those commercialised by Siemens (Germany), ITM power (UK), Proton Onsite (USA) and Hydrogenics (Canada). A standard approach for protecting stainless steel BPPs for PEMFCs is to apply a coating

with high corrosion resistance and excellent electronic properties [18,19]. Conductive thin films, such as Au [20], TiN [21], TiN/C [22], TaN [23], and SnO<sub>2</sub>:F [24], have been widely evaluated to protect PEMFC BPPS from corrosion. However, all these coatings fail to provide the necessary protection against corrosion in a simulated PEMFC cathode environment, especially at high potentials. It is therefore expected that these coatings will have even less durability when used in PEM electrolysis.

To the best of our knowledge, the use of thermally sprayed coatings for the stainless steel BPPs of a PEM electrolyser has not yet been explored. We report herein an electrically conductive and corrosion-resistant bi-layer coating for this application. It was deposited by successive VPS and PVD magnetron sputtering of Ti and Pt, respectively. The thermal spraying technique is very suitable for producing Ti coatings [25–27], although the resulting layers were presumably not dense enough and therefore oxidised during the thermal deposition process. Moreover, such coatings have never been evaluated under PEM electrolyser operation conditions. The coatings reported here were characterised by scanning electron microscopy (SEM), atomic force microscopy (AFM), X-ray diffraction (XRD), and X-ray photoelectron microscopy (XPS). Subsequently, the ICR was measured at various compaction forces. Lastly, an exhaustive electrochemical evaluation was carried out on the coatings in both simulated and real PEM electrolyser environments.

## **2. Material and methods**

### *2.1. VPS/PVD of coatings*

The development of the thermally sprayed Ti coatings was reported elsewhere [28]. Briefly, titanium coatings were deposited via VPS on sandblasted Crofer<sup>®</sup> 22 H stainless steel plates of 47 x 47 x 1 mm<sup>3</sup> from ThyssenKrupp VDM (Werdohl, Germany). The substrate was pre-heated to 250 °C in the vacuum chamber before the spraying procedure. Several parameters such as the type of

plasma torch nozzle, the powder feeding rate, and the plasma gas flow rates of Ar, N<sub>2</sub> and H<sub>2</sub> were carefully chosen to achieve a plasma enthalpy ( $h$ ) of 21.3 MJ kg<sup>-1</sup>. A torch sweep rate of 500 mm s<sup>-1</sup> was used. Titanium powder (grade 1, grain size < 45 μm) from TLS Technik Spezialpulver (Bitterfeld-Wolfen, Germany) was sprayed in the VPS system at a chamber pressure of 50 mbar to avoid the oxidation of Ti. Several coatings with different numbers of Ti layers were thermally sprayed on the stainless steel substrates by varying the number of torch sweeps or coating runs. Lastly, a full densification of the Ti coating was carried out using a capillary sealing process.

Pt thin films were deposited on the plasma-sprayed Ti coatings (8 wt% Pt/Ti) via PVD magnetron sputtering using a pilot instrument from Von Ardenne Anlagentechnik (Dresden, Germany). The surface of the Ti layer was finely sanded, cleaned and argon-etched prior to the deposition of the Pt coating to remove the passive layer of TiO<sub>2</sub> that forms on Ti in air. The Ar<sup>+</sup> etching step was carried out by applying 100 V for 5 min under a chamber pressure of 1 x 10<sup>-1</sup> mbar. A nominal coating thickness of approximately 1.8 μm was aimed for by applying 270 W to the Pt-target for 10 min under a chamber pressure of 4 x 10<sup>-3</sup> mbar.

## 2.2. SEM, AFM, XRD, XPS analyses

Cross-section images of the Pt/Ti coatings before and after corrosion measurements were taken with an SEM Zeiss ULTRA plus (secondary electron detection) with charge compensation. The accelerating voltage was 15 kV with a working distance of 8.4 mm. For the AFM investigations, a Bruker Multimode 8 AFM (Karlsruhe, Germany) equipped with a Nanoscope V controller and an x-y closed loop scanner with an open loop z-axis (nPoint, USA) was used in a quantitative nano-mechanical tapping mode (QNM<sup>TM</sup>, Bruker Corp.). The measurements were performed using PtIr coated tips (PPP-NCHPT, 42 N m<sup>-1</sup>; Nanosensors). The samples were fixed to the sample holder with a silver epoxy adhesive.

The XPS measurements were performed using a Thermo Scientific ESCALAB 250 ultra-high vacuum facility with a base pressure of  $1 \times 10^{-9}$  mbar. The depth profiles were conducted with gradual argon-sputtering and subsequent XPS analysis. For the sputtering process, a Thermo EX05 ion gun was used with the following settings:  $2 \times 10^{-8}$  mbar Ar partial pressure, 2 kV acceleration voltage and 10 mA emission current yielding to an  $\text{Ar}^+$  current of  $4.4 \mu\text{A}$  in an area of  $3 \times 4 \text{ mm}^2$  (sputter current density:  $j_{\text{Ar}} = 0.37 \mu\text{A}/\text{mm}^2$ ). An Al-K $\alpha$  X-ray source (Thermo XR4) and a small-area lens mode ( $0.8 \text{ mm}^2$ ) served to ensure that the measuring spot was entirely within the sputtering crater. The atomic concentrations of elements in the studied samples were quantified using the XPS sensitivity factors provided by Thermo Scientific. A Shirley function was used for peak background correction. The sputtering yields were not calibrated and hence, the depth profiles were plotted as a function of sputter time (or synonymously, etching time) only. All XPS experiments were performed at room temperature.

The crystalline properties of the coatings were studied by measuring the XRD spectra from the top and cross-sections of the samples in reflection mode. A D8 Discover GADDS diffractometer with a V $\text{ANTEC}$ -2000 area detector was used for this purpose. The X-ray source consisted of a tuned monochromatic and parallel X-ray beam (Cu-K $\alpha$ ) with an accelerating voltage of 45 kV and a tube current of 0.650 mA. The tube collimator aperture was 1 mm in diameter. Each XRD pattern was measured in four frames with an exposure time of 180 s per frame and a step size of  $2\theta = 23^\circ$  between frames (first frame  $\theta_1 = \theta_2 = 12^\circ$ ). Rietveld analysis of the spectra was performed with the software Topas (Bruker).

### *2.3. ICR measurements*

The ICR of the coatings with an interconnecting element was determined following the method reported elsewhere [24]. In short, coated samples were placed between two pieces of Toray gas diffusion layer (GDL) paper. This sandwich-like arrangement was compressed between two Cu cylinders by a hydraulic press. The surface of the cylinders in contact with the Toray paper was

cleaned with diluted  $\text{H}_2\text{SO}_4$  prior to each measurement. The positive and negative terminals of a power supply were connected to the Cu cylinders, and an electrical current of 5 A was applied. The voltage difference across the Cu terminals was measured at various compaction pressures. The ICR between the Toray paper and the coating was measured by fitting the recorded signal to a reported equivalent electrical circuit [29].

### *2.3 Corrosion evaluation*

Electrochemical measurements were performed using an Autolab PGSTAT12 potentiostat/galvanostat and a three-electrode cell containing approximately 1 l of 0.5 M  $\text{H}_2\text{SO}_4$  heated to 65 or 80 °C, depending on the experiment to be performed. The electrolyte was saturated with high-purity  $\text{O}_2$  (Praxair) for 20 min to simulate the oxidative environment of the anode of a PEM electrolyser. A platinum foil and a reversible hydrogen electrode (RHE) from HydroFlex® served as the counter (CE) and reference electrode (RE), respectively. As the working electrode (WE), a sample holder was manufactured from polyether ether ketone (PEEK) and 18 x 18 mm<sup>2</sup> samples of the coated plates were tightly mounted with a cap and a silicone O-ring. This cap had a 1 cm<sup>2</sup> hole and another O-ring that exposed this area to the electrolyte while keeping the rest of the coating dry. Additionally, samples of uncoated Crofer® and a Ti foil (99.99+ Alfa Aesar) with the same surface finish as that of the Ti-coated samples were electrochemically evaluated.

### *2.4. PEM electrolyser tests*

The anode electrode plate for a 25 cm<sup>2</sup> PEM electrolyser cell with a serpentine mono-channel flow field design was manufactured from stainless steel 1.4301 and then coated with Pt/Ti. A cathode electrode plate with the same design was coated with Au via electro-deposition. A sintered porous Ti plate and carbon paper served as current collectors for the anode and cathode, respectively. A commercial MEA with a CSN115 membrane, an Ir-based anode and a Pt-based cathode was employed. The MEA was flooded overnight with deionised water (DI, 0.2  $\mu\text{S cm}^{-1}$ ) to hydrate the

membrane. An in-house testing station was built for the PEM electrolyser measurements with O<sub>2</sub> and H<sub>2</sub> gas separators, a power supply, a control unit, a computer and a thermostat. The water was supplied only to the anode side of by a diaphragm pump at a flow rate of 1.2 ml s<sup>-1</sup>. PEM electrolysis measurements were carried out at 1 bar.

### **3. Results and discussion**

#### *3.1. Physical characterisation and electrical properties*

The Pt/Ti coatings were characterised by SEM and AFM. Figure 2a and 2b schematically show cross-sections of Pt/Ti/ss and Pt/ss samples, respectively, indicating the areas that were subjected to corrosion evaluation, labelled the corrosion zones in the scheme. Figure 2a and 2b highlight the only difference between the two samples, which is a relatively thick layer of Ti between the Pt and the Crofer<sup>®</sup> substrate. Figure 2b also schematises the phenomenon of pitting corrosion that occurred on Pt/ss but not on the Pt/Ti/ss sample. Photos of the Pt/Ti/ss and Pt/ss samples after the corrosion evaluation are presented in Figure 2c and 2d, respectively. No difference between the corroded (A) and non-corroded (B) areas of the Pt/Ti/ss sample can be observed with the naked eye. Conversely, it is quite clear that the central area (circle, A) of the Pt/ss sample has been severely damaged after the corrosion tests. Severe pitting corrosion led to the formation of small holes under the Pt layer. The rest of the surface of the samples (B) was effectively protected from corrosion thanks to the silicone O-ring sealing the sample holder. Thus, this area can be used to characterise the original coating before performing corrosion measurements.

SEM analysis on cross-sections of the coated samples was carried out to study the morphology and observe the negative effects of corrosion in the simulated PEM electrolyser environment. Figure 3a and 3b show the Pt/Ti coating on the Crofer<sup>®</sup> substrates before and after electrochemical testing. In the images, the coating is dense, and all the Ti particles from the feedstock powder that was used in the VPS process have been melted. The thickness of the Ti coating (16 coating runs) is approximately 120 µm both before and after the corrosion test. Energy-dispersive X-ray

spectroscopy (EDX) analysis of the surface of the coating (shown in Figure S1 of the supporting information) was performed on the surface of the coating, which revealed that the Ti coating was composed of ca. 97 wt% Ti. The remaining 3% corresponds to impurities from the SiC and Al<sub>2</sub>O<sub>3</sub> suspensions used during the sanding and polishing process, respectively.

The thin bright line on top of the Ti coating shown in Figure 3a and 3b corresponds to the Pt film that was deposited by PVD magnetron sputtering. Magnified images of the Pt layer before and after the electrochemical measurements are presented in Figure 3c and 3d, respectively. By measuring the thickness of the Pt layer at different locations, the average Pt coating thickness was found to be ca. 1.14 μm thick before and 1.07 μm after the corrosion tests. This slight decrease cannot be attributed to dissolution of PtO<sub>2</sub>, and it is much more likely due to experimental error in measuring the thickness. No sign of degradation, such as peeling, pitting corrosion or pinhole formation, can be observed in the SEM images.

In contrast, the sample without the thermally sprayed Ti coating, namely Pt/ss, experienced severe degradation, which can be observed in the cross-sectional SEM image presented in Figure 3f and the corresponding close up in Figure 3h. An image of a sample before corrosion measurements is presented in Figure 3e and a cutaway view in Figure 3g. A substantial amount of the Crofer<sup>®</sup> under the Pt coating was removed due to acute pitting corrosion. Thereafter, Fe<sup>2+</sup> and Cr<sup>3+</sup> were released into the aqueous electrolyte that was used for the corrosion measurements. In a real PEM electrolyser environment, these ions would poison the MEA, thereby causing a gradual and irreversible increase in the cell voltage [15,16]. Furthermore, the surface area below the almost free-standing Pt layer was enlarged because of the pitting corrosion. This effect was also reflected in the electrochemical measurements, which will be discussed in the next section.

AFM measurements provide topography information on a smaller length scale. Figure 4a and 4b show AFM images of Pt/ss before corrosion for the topography and the peak force, indicating sharp height differences and therefore enhancement of surface structures. The Pt layer is mostly smooth

except for scratches in two directions on the order of 20 - 100 nm in depth caused by polishing the stainless steel. The image also shows some undefined grains which may be impurities. For the case of Pt/Ti/ss before corrosion in Figure 4c and 4d, these scratches are still apparent with depths of 15 – 20 nm, but these surface structures are diminished by the Ti layer. The surface of this sample shows larger heterogeneities with crevices (350 nm) and elongated holes of approximately 100 nm. These characteristics are most likely a consequence of the splat structure of the thermally sprayed Ti coating with structure relaxations due to mechanical stresses induced by fast cooling.

The AFM analysis on Pt/Ti/ss after the corrosion tests is shown in Figure 4e, 4f and 4g for topography, peak force and current, respectively. The oxidation of Ti beneath the Pt, with the corresponding volume extension, further diminished the substrate scratches, which are now hardly visible in the images. The high potentials are an indication of the heterogeneous oxide growth that is exhibited by grain accumulation on the investigated surfaces. These areas show a lower electronic conductivity, as shown in the current image (Figure 4g) of the same region. However, large conductive areas remain, which may be sufficient for effective electrical contact with the current collector of the PEM electrolyser. The AFM investigations on Pt/ss after corrosion show a deformed but homogeneous surface with many small grains (see Figure S2 of the supporting information). Indeed, clear evidence of acute pitting corrosion in the stainless steel substrate can be observed in the AFM topography images of the corroded Pt/ss sample.

The structural properties of the as-prepared Pt and Ti coatings were analysed by XRD. Figure 5a shows the XRD spectra measured in reflection mode from the coated surface of Pt/Ti/ss and Ti/ss. In both spectra, the stainless steel substrate is unobservable due to the high density and thickness of the layers. The spectra fit the pattern of face centred cubic Pt (Powder diffraction file, PDF: 01-087-0636, S.G. Fm-3m) and hexagonal Ti (PDF: 00-044-1294, S.G. P63/mmc). The lattice parameters and mean crystallite size of Pt and Ti layers are summarised in Table 1. The high relative intensity of the (111) reflex demonstrates that the Pt nano-crystallites are preferably orientated in this specific

direction. The fitted spectra and further information on the spectra refinement can be found in the supporting information.

The XPS spectra of the Ti2p and O1s binding energy regions of as-prepared Pt/Ti/ss are shown in Figure 5b and 5c, respectively. The spectra of an anodised sample of Ti/ss are presented as dashed lines for comparison purposes. The anodisation enhances the crystallisation of TiO<sub>2</sub>, which significantly reduces the thickness of the mixed TiO<sub>2</sub>/Ti phase (see Figure S5a of the supporting information). For Pt/Ti/ss, the peaks from Ti start emerging after sputtering times of approximately 150 minutes as a result of the removal of the Pt layer during the ion etching process (compare with Figure S5b in the supporting information). The oxygen to titanium ratio of Pt/Ti/ss (after removal of Pt) was found to be 28 times lower than the corresponding ratio of a non-anodised Ti/ss sample, suggesting the absence of amorphous TiO<sub>2</sub> between the Pt and Ti layer. Furthermore, the Ti2p peak positions of Pt/Ti/ss (Ti2p<sub>3/2</sub> at 454 eV and Ti2p<sub>1/2</sub> at 460 eV) and anodised Ti/ss (Ti2p<sub>3/2</sub> at 459 eV and Ti2p<sub>1/2</sub> at 465 eV) in Figure 5b unambiguously indicate pure Ti and TiO<sub>2</sub>, respectively [30]. The positions of these peaks further demonstrate that there is no measurable TiO<sub>2</sub> between the Pt and Ti layers, thereby confirming that the TiO<sub>2</sub> was entirely removed in the course of the PVD process described in the experimental section. In the case of O1s (Figure 5c), the peak shift between these two samples is much smaller; however, the O1s peak of the Pt/Ti/ss sample is located at a binding energy approximately 1 eV higher than the corresponding signal of the Ti/ss. Neither the XRD nor XPS spectra of Pt/Ti/ss showed any trace of TiO<sub>2</sub> after corrosion measurements, indicating that the oxide layer under the Pt grew only on small areas and did not crystallise.

In general, the ICR of coatings for PEMFC bipolar plates is measured using a carbon GDL [20,29]. However, in-state-of-the-art PEM electrolyzers, a sintered Ti disc is used as the anode current collector [31], which is not as compressible as the carbon GDL. Thus far there is no generally accepted method in the field of PEM electrolysis for measuring the ICR of a coated BPP. Nevertheless, the ICR parameter was used to characterise the electrical properties of the coatings presented in this work.

The ICR under various compaction pressures on the as-prepared Ti/ss, Pt/ss and Pt/Ti/ss samples is presented in Figure 5d. The ICR of the Ti/ss sample gradually decreases as the compaction pressure increases. The high ICR at low pressures is a clear indication of the passivation of the coating due to the well-known dielectric properties of the semiconducting oxide layer on Ti [32]. Secondly, the ICR of Pt/ss and Pt/Ti/ss, measured at a compaction pressure of at  $181 \text{ N cm}^{-2}$ , is approximately 96 and  $100 \text{ m}\Omega \text{ cm}^{-2}$ , respectively. The applied force on the current collector corresponds to a bolt torque of slightly more than 10-15 N m depending on the gasket material of the electrolyser [33]. At higher compaction forces, the ICR remained virtually the same. This result indicates that a  $120 \mu\text{m}$  thick Ti coating does not contribute significantly to the through-plane electrical resistivity of the bilayer coating. It also shows that the Ti particles did not oxidise during the VPS deposition, in spite of the high temperature of the plasma. In addition, the ion etching procedure prior to the PVD of Pt removed the  $\text{TiO}_2$  on the Ti, as already demonstrated by XPS. Thus, the thin layer of precious metal prevented any subsequent passivation of the Ti layer when in contact with atmospheric air.

### 3.2. Half-cell electrochemical measurements

#### 3.2.1. Ti-coated stainless steel

The thermally sprayed Ti coatings without Pt on the surface were evaluated in a simulated PEM electrolyser environment ( $E \leq 2 \text{ V}$ ,  $\text{pH} = 0$ ,  $T = 65 - 80 \text{ }^\circ\text{C}$ ). Figure 6a shows the first and second linear voltammetry scans performed on Ti/ss at  $1 \text{ mV s}^{-1}$  in  $\text{O}_2$ -saturated  $0.5 \text{ M H}_2\text{SO}_4$  at  $65 \text{ }^\circ\text{C}$ . This sample was coated by 16 coating runs which led to a Ti layer thickness of  $120 \mu\text{m}$ . Similarly, a high-purity Ti foil and an uncoated plate of stainless steel were measured for comparison purposes. The potentiodynamic curve of the Ti/ss sample shows the typical oxidation behaviour from Ti to amorphous  $\text{TiO}_2$  at ca.  $0.1 \text{ V vs. RHE}$ , followed by a steady passivation of the coating up to  $2 \text{ V vs. RHE}$ , before the dielectric breakdown [34]. At the end of the first scan, a compact amorphous oxide layer covered the Ti coating as a result of the anodisation phenomenon in diluted sulphuric acid [35]. During the second scan, the current density increased somewhat in the cathodic region. In

addition, the corrosion current ( $j_{corr}$ ) decreased almost one order of magnitude, and the corrosion potential ( $E_{corr}$ ) was positively shifted by approximately 0.13 V.

The high-purity Ti foil, which was tested under the same experimental conditions, showed very similar potentiodynamic curves as the Ti/ss sample. This result is in good agreement with the EDX analysis in the supporting information, which shows that the thermally sprayed Ti coating is comparable to the bulk material. The uncoated Crofer<sup>®</sup> sample presents its well-known potential windows corresponding to the active, passive, and transpassive corrosion zones of stainless steel in sulphuric acid [36]. If stainless steel is the base material for a PEM electrolyser stack, then the transpassive region is of special importance. A large anodic wave appears at ca. 1 V vs. RHE, which corresponds to the oxidation of Fe<sup>2+</sup> to Fe<sup>3+</sup>. Beyond this potential, the oxygen evolution reaction (OER) occurs, and the applied current density reaches a plateau at 1.4 V vs. RHE. In contrast, the current density at 2 V vs. RHE for Ti/ss is ca. 10,000 times lower, indicating that the thermal spraying coating fully protected the substrate from corrosion.

Chronoamperometric measurements at  $E_{const} = 2$  V vs. RHE were performed to further evaluate the corrosion resistance of the thermally sprayed Ti coating on stainless steel. Figure 6b presents the potentiodynamic characteristics of Ti/ss (32 coating runs) before and after a 24 h chronoamperometric test. The current-time transient is shown in the inset of Figure 6b. Both experiments were carried out in O<sub>2</sub>-saturated 0.5 M H<sub>2</sub>SO<sub>4</sub> at 80 °C. Similar to Figure 6a, the cathodic current of Ti/ss increased substantially after the chronoamperometric test, resulting in a high production of H<sub>2</sub> bubbles. The shape of the chronoamperometric curve, in the inset of Figure 6b is characteristic of the anodisation process of Ti [37]. Note that there is no indication of corrosion of the stainless steel substrate in Figure 6b, even after exposure to 2 V vs. RHE for 24 h. This testing period is much longer than what is normally reported in the literature on coatings for bipolar plates of PEMFC [21,23,24]. As shown in the inset of Figure 6b, the current transient does not decrease any further with time, indicating that the TiO<sub>2</sub> layer does not grow further on the Ti.

In another experiment, polished samples of bulk Ti (i.e., foil) and Ti/ss (8 coating runs) were anodised for 14.5 h at a constant potential of 2 V vs. RHE in O<sub>2</sub>-saturated 0.5 M H<sub>2</sub>SO<sub>4</sub> at 80 °C. Subsequent chronoamperometric measurements were performed on both samples under the same conditions as described above. The current-time transient in Figure 6c showed virtually no difference in the electrochemical responses of bulk Ti and Ti/ss. The inset of Figure 6c presents a cross-sectional SEM image of the coated sample used for the measurements, and in this case the Ti coating is ca. 60 µm thick. The most relevant conclusion from the previous chronoamperometric test is that the massive high-purity Ti can feasibly be replaced by a 60 µm thick thermally sprayed Ti coating. It possesses at least the same properties and electrochemical characteristics as bulk Ti. Therefore, the amount of this metal in the PEM electrolyser stack can be largely diminished. Moreover, the costly process of producing a flow field on a BPP can be minimised as machining stainless steel is easier than machining Ti.

### 3.2.2. Pt/Ti-coated stainless steel

The corrosion resistance of a thermally sprayed Ti coating on stainless steel was discussed in the previous sub-section. While the cost of a Ti-coated BPP is lower than the cost of a BPP completely made of Ti, the electrolyser would experience degradation due to the formation of TiO<sub>2</sub> on the areas of the coating in contact with the current collector. An electro-deposited micro-layer of Pt on the BPPs of a URFC can reduce the formation of TiO<sub>2</sub>, thus improving the performance of the electrochemical device [11]. However, a thin layer of TiO<sub>2</sub> is formed between Pt and Ti when using electrodeposition technique. As shown below, stable and dense Pt layers can be effectively achieved by PVD magnetron sputtering without significant TiO<sub>2</sub> growth between the Pt and the sprayed Ti coating.

The Pt/Ti coatings were evaluated for corrosion resistance under the simulated operation conditions of a PEM electrolyser. For an exact comparison of Pt/Ti/ss and Pt/ss, the characteristics of the samples were strictly controlled, namely (i) the same sputtering time and deposition parameters for

Pt on uncoated and Ti-coated stainless steel; (ii) the same thickness of the thermally sprayed Ti coating, i.e., ca. 120  $\mu\text{m}$  (16 coating runs); and (iii) the same surface finishing prior to Pt deposition. No polishing suspensions were used for these samples to avoid abrasive impurities that could remain at the Pt and Ti interface.

The chronoamperometric characteristics of the Pt/ss, Ti/ss and Pt/Ti/ss samples measured under  $E_{\text{const}} = 2 \text{ V vs. RHE}$  in  $\text{O}_2$ -saturated 0.5 M  $\text{H}_2\text{SO}_4$  at 65  $^\circ\text{C}$  is shown in Figure 7a. This temperature was selected to match the experimental conditions of the PEM electrolyser test as closely possible, which is discussed in the next section. The resulting current-time transients are quite different from each other. The high current densities observed for the Pt-coated samples are attributed to the generation of molecular oxygen on the surface of the electrodes. In contrast, for Ti/ss, no generation of  $\text{O}_2$  bubbles was observed at all. In the case of Pt/ss, the measured current density increased linearly at a rate of ca. 1.7  $\text{mA h}^{-1}$ . This slope is a clear indication of pitting corrosion, similar to how it occurs on samples coated with TiN [21] and  $\text{SnO}_2\text{:F}$  [24] when evaluated in the simulated environment of a PEMFC cathode. The  $[\text{Fe}^{2+}]$  was found to be approximately 27.7 ppm using a photometer at the end of the chronoamperometric test.

In the case of Pt/Ti/ss, the current increased during the first two hours, reaching a maximum value after ca. 2.8 h, and it decreased steadily afterwards. This increase in the current density might be associated with an electrochemical cleaning of the Pt surface and an erosion of the layer by small  $\text{O}_2$  bubbles. Thereafter, monolayers of  $\text{PtO}_x$  begin to nucleate as a result of the anodisation of the precious metal at high potentials [38]. In contrast, the generated current density of Ti/ss is much lower than that of Pt/Ti/ss, indicating that the uncoated Ti was passivated. The inset of Figure 7a shows a cutaway view of the chronoamperometric characteristic of Ti/ss. After 6 h, the Pt/ss sample already showed changes in colour and roughness, as shown in Figure 2d, which indicates serious damage to the Pt coating. The same experiment was also carried out on uncoated stainless steel, but at 1.5 V vs. RHE, but the experiment was stopped after only 2 h, as the electrolyte was already contaminated with ca. 100.8 ppm of  $\text{Fe}^{2+}$ . The results are presented in the supporting information.

Figure 7b shows the potentiodynamic curves of the Pt-coated samples before and after the chronoamperometric test in Figure 7a. For the sake of clarity, only the Ti/ss sample after the anodisation was included in the plot. Table 2 summarises some electrochemical parameters calculated from the potentiodynamic curves in Figure 7b. The polarisation resistance ( $R_p$ ) was determined using the following equation [39]:

$$R_p = \frac{\beta_a \beta_c}{2.3 j_{corr} (\beta_a + \beta_c)} \quad (1)$$

where  $\beta_a$  and  $\beta_c$  are the anodic and cathodic Tafel slopes, respectively, and  $j_{corr}$  is the corrosion current density. From 0.3 V up to 1.2 V vs. RHE, the characteristics of the Pt/ss and Pt/Ti/ss are very similar, having an  $E_{corr}$  of 0.92 V vs. RHE and a  $\beta_c$  of ca. 20 mV dec<sup>-1</sup>. The potential window between 0.3 V and 0.9 V vs. RHE is dominated by the oxygen reduction reaction (ORR) on Pt, and the formation of PtO<sub>x</sub> begins above this range. However, the  $j_{corr}$  and  $\beta_a$  of Pt/ss are almost twice those of Pt/Ti/ss, indicating that stainless steel is being corroded in the Pt/ss sample. Moreover, at 1.2 V vs. RHE, a low anodic current begins to emerge gradually for Pt/ss but not for Pt/Ti/ss. Subsequent anodic scans on Pt/ss clearly show how the electrochemical surface area (ECSA) of the stainless steel beneath the Pt increases gradually. For the sake of clarity, only the first (s1) and fifth (s5) scans are shown in Figure 7b; the remaining data are available in Figure S6b of the supporting information. These results suggest that a thermally sprayed Ti coating is not necessary below 1.2 V, as the Pt layer is sufficient to protect the stainless steel substrate from corrosion up to a certain degree. However, above this potential, Fe<sup>2+</sup> and Cr<sup>3+</sup> begin to dissolve out of the Crofer<sup>®</sup> substrate, thus contaminating the electrolyte. Hence, the unequivocal protection offered by the Pt/Ti coating against corrosion, even at higher potentials, makes it superior to the Pt layer deposited on stainless steel. Note that PVD coatings have been established as the preferred method for coating the BPPs of a PEMFC [19]. However, the results obtained with the Pt/ss sample explain the lack of previous reports on PVD coatings for stainless steel BPPs for PEM electrolyzers.

After performing the chronoamperometric test shown in Figure 7a, the Pt/ss sample exhibited very similar electrochemical characteristics to those of uncoated stainless steel above 1.4 V vs. RHE (see Figure 6a). Therefore, the OER is now taking place on the corroded voids of the stainless steel below the Pt layer. The corroded zones are shown in the cross-section SEM image in Figure 3d. In contrast, the current-potential curves of the Pt/Ti/ss were virtually the same before and after the chronoamperometric test, thus demonstrating that the bilayer coating fully protected the Crofer<sup>®</sup> substrate over an extended period of time. Furthermore, the  $R_p$  of Pt/Ti/ss remained almost the same, while for the uncoated and Ti/ss samples,  $R_p$  increased considerably as a result of the growth of the oxide layer. These results indicate that the Pt/Ti coating preserves its high conductivity even after being polarised at 2 V vs. RHE for 6 h. No traces of  $\text{Fe}^{2+}$  were detected in the electrolyte at the end of the electrochemical experiment for either Ti/ss or Pt/Ti/ss.

All electrochemical tests were carried out on flat surfaces. However, completely protecting the complex geometry of the flow fields of a BPP is still an area of concern. Cross-sections (not shown) of proprietary BPPs with the Pt/Ti coating revealed that the protective layer covers all regions of the manifolds, the exposed 3D areas of the flow field, the inlet/outlet holes, edges, corners, and even some regions of the backside of the BPP.

### *3.3. Evaluation of the Pt/Ti coating in a PEM electrolyser*

The Pt/Ti coating was tested in a 25 cm<sup>2</sup> PEM electrolyser operating at nominal conditions of temperature, pressure and applied loading. The Pt/Ti coating was deposited on the stainless steel anode EH. Figure 8 shows the cell voltage vs. current density characteristics at 67 and 76 °C, promptly measured after the overnight activation procedure of the MEA described in the experimental section. The left inset of Figure 8 is a photo of the coated EH with a serpentine monochannel flow field. A cell potential of 1.75 V was measured at 1 A cm<sup>-2</sup>, which corresponds to the standard performance of state-of-the-art PEM electrolysers [7,40]. At current densities higher than 1.2 A cm<sup>-2</sup>, the forward scan differs from the backward scan, which indicates that the cell exhibits

mass transport issues. However, this phenomenon is related to the characteristics of the current collectors or the flow field design rather than the O<sub>2</sub>-bubble/water management functionality of the Pt/Ti coating.

The PEM electrolyser was constantly loaded at 1.2 A cm<sup>-2</sup> for almost 200 h. The right inset of Figure 8 presents the cell voltage and temperature as a function of the operating time. The initial cell voltage was approximately 2 V but increased sharply up to 2.12 V after only 5 h of testing. This rapid degradation apparently contradicts the results discussed in the previous section. However, this negative effect can be easily reversed simply by changing the DI water in the gas separators of the system. The degradation in the MEA caused by Fe<sup>2+</sup> cannot be reversed without an acid treatment, as reported elsewhere [16]. Therefore, the momentary increase in the cell potential vs. time is not an indication of the failure of the Pt/Ti coating deposited on the stainless steel EH. The average degradation rate of the PEM electrolyser cell was 26.5 μV h<sup>-1</sup>, which is ca. 10 μV h<sup>-1</sup> lower the previously reported degradation rate for a 9-cell stack with titanium BPPs operating constantly at 0.5 A cm<sup>-2</sup> [15]. The results of a much longer test and post-mortem analysis will be reported in a separate study.

### *3.4. Cost reduction and further improvement*

An estimation of the cost of coating a large volume of stainless steel BPPs with Ti was calculated, taking into consideration expenses from equipment consumables, feedstock powder and working hours. The details of the cost calculation are given in the supporting information. Briefly, coating a stainless steel BPP of ca. 1000 cm<sup>2</sup> (dimensions: 30 x 30 x 0.3 cm<sup>3</sup>) with Ti would cost 3.13 USD per plate or 30.80 USD m<sup>-2</sup> (March 2014). It is possible to fabricate a 1 MW PEM electrolyser stack with 25 of these plates. However, the cost of the VPS process greatly depends on the area to be coated and the production volume. Currently, coating a single 1 m<sup>2</sup> BPP is significantly more expensive than coating 10 plates with an area of 1000 cm<sup>2</sup> each because handling problems in the production process worsen with the increasing sample size, and the investment capital is much

higher for a large area coating facility. The cost of the substrates and surface processing with Pt or other precious metals is not included in the estimation.

The use of expensive coating metals and two separate deposition techniques in the manufacturing process ostensibly does not represent a significant reduction in cost. However, the Pt/Ti coating contains only approximately 8 wt% of Pt, and both deposition techniques are widely implemented in the industry. Because the Pt layer did not experience significant degradation, the amount of this precious metal can be decreased to a few monolayers deposited on the thermally sprayed Ti coating. Moreover, the surface of the Ti coating can be modified with less expensive coatings such as Au [14], boron-doped diamond (BDD) [41] or Ir-Ta [10]. Finally, it is important to consider the following: (i) No corrosion of the stainless steel substrate was observed using the Ti coating reported herein, and (ii) the BPP of PEM electrolyser have no weight or thickness limitations such as those for fuel cells. Therefore, it is quite possible to use less noble but cheaper and more conductive metals such as ss314, Cu or Al as base materials for the PEM electrolyser stack. Table 3 summarises the cost and conductivities of these metals in comparison with high-purity Ti. By replacing Ti with ss314, Cu or Al as the BPP base material, the manufacturing cost would be reduced by 56%, 61%, and 74%, respectively. Another potential cost advantage of these materials comes from machining or chemically etching the flow field onto these metals.

#### **4. Conclusions**

We have reported a conductive and corrosion-resistant coating for stainless steel bipolar plates for a PEM electrolyser. This work showed that a 60  $\mu\text{m}$  thick, dense and robust Ti coating produced by VPS is sufficient to provide the necessary protection in the anodic environment of a PEM electrolyser. A highly conductive and dense Pt thin film subsequently coated via PVD magnetron sputtering, which resulted in a 50-fold lower thickness, can prevent the passivation of the Ti coating. Thus, a comprehensive solution to the issue of producing corrosion-resistant stainless steel bipolar plates has been demonstrated, and the cost of the stack can be reduced. However, the VPS

coating thickness should be decreased even further (e.g., 30  $\mu\text{m}$ ) to further minimise the production costs of a large volume of bipolar plates. Reducing the thickness, eliminating precious metals, and substituting cheaper metals for the stainless steel are all subjects of our on-going research.

Lastly, the coating strategy presented in this work can also be used to protect low-cost bipolar plates for PEMFCs and redox flow batteries, in which corrosion under high potentials is a critical issue. Producing coatings that meet the requirements of a PEM electrolyser in only one step is still a challenge, whether performed by VPS, PVD magnetron sputtering or other techniques.

### **Acknowledgements**

The authors acknowledge the Federal Ministry for Economic Affairs and Energy (BMWi) for financially supporting the project No. 0325440A. The authors are also grateful to Günter Roth, Gudrun Steinhilber, and Ina Plock for spraying the VPS coatings, preparing the samples for analysis, and the acquiring the SEM images, respectively. Finally, we thank Thomas Kupke for manufacturing the sample holder for corrosion measurements.

### **References**

- [1] A. Sternberg, A. Bardow, *Energy Environ. Sci.* (2015) 389.
- [2] P. Millet, S. Grigoriev, in: L.M.G.A.M. Diéguez (Ed.), *Renew. Hydrog. Technol.*, Elsevier, Amsterdam, 2013, pp. 19–41.
- [3] Fuel Cells and Hydrogen Joint Undertaking, *Commercialisation of Energy Storage in Europe, A Fact-Based Analysis of the Implications of Projected Development of the European Electric Power System towards 2030 and beyond for the Role and Commercial Viability of Energy Storage*, 2015.
- [4] K.E. Ayers, E.B. Anderson, C. Capuano, B. Carter, L. Dalton, G. Hanlon, J. Manco, M. Niedzwiecki, *ECS Trans.* 33 (2010) 3.
- [5] K.E. Ayers, C. Capuano, E.B. Anderson, *ECS Trans.* 41 (2012) 15.
- [6] L. Bertuccioli, A. Chan, D. Hart, F. Lehner, B. Madden, E. Standen, *Study on Development of Water Electrolysis in the EU by E4tech Sàrl with Element Energy Ltd for the Fuel Cells and Hydrogen Joint Undertaking*, 2014.
- [7] M. Carmo, D.L. Fritz, J. Mergel, D. Stolten, *Int. J. Hydrogen Energy* 38 (2013) 4901.

- [8] H.G. Kim, L.K. Kwa, W. Han, L.K. Kwac, in: *Int. Conf. Power Energy Syst. Lect. Notes Inf. Technol.* Vol.13, 2012, pp. 373–379.
- [9] C.K. Jin, M.G. Jeong, C.G. Kang, *Int. J. Hydrogen Energy* (2014) 1.
- [10] J.-T. Wang, W.-W. Wang, C. Wang, Z.-Q. Mao, *Int. J. Hydrogen Energy* 37 (2012) 12069.
- [11] H.-Y. Jung, S.-Y. Huang, B.N. Popov, *J. Power Sources* 195 (2010) 1950.
- [12] S.S. Dhrab, K. Sopian, M.A. Alghoul, M.Y. Sulaiman, *Renew. Sustain. Energy Rev.* 13 (2009) 1663.
- [13] D.R. Hodgson, B. May, P.L. Adcock, D.P. Davies, *J. Power Sources* 96 (2001) 233.
- [14] H.-Y. Jung, S.-Y. Huang, P. Ganesan, B.N. Popov, *J. Power Sources* 194 (2009) 972.
- [15] S. Sun, Z. Shao, H. Yu, G. Li, B. Yi, *J. Power Sources* 267 (2014) 515.
- [16] X. Wang, L. Zhang, G. Li, G. Zhang, Z. Shao, B. Yi, *Electrochim. Acta* 158 (2015) 253.
- [17] J. André, L. Antoni, J.P. Petit, *Int. J. Hydrogen Energy* 35 (2010) 3684.
- [18] R.A. Antunes, M.C.L. Oliveira, G. Ett, V. Ett, *Int. J. Hydrogen Energy* 35 (2010) 3632.
- [19] M.C.L. de Oliveira, G. Ett, R.A. Antunes, *J. Power Sources* 206 (2012) 3.
- [20] A. Kumar, M. Ricketts, S. Hirano, *J. Power Sources* 195 (2010) 1401.
- [21] Y. Wang, D.O. Northwood, *J. Power Sources* 191 (2009) 483.
- [22] H. Sun, K. Cooke, G. Eitzinger, P. Hamilton, B. Pollet, *Thin Solid Films* 528 (2013) 199.
- [23] C. Choe, H. Choi, W. Hong, J.-J. Lee, *Int. J. Hydrogen Energy* 37 (2012) 405.
- [24] H. Wang, J.A. Turner, *J. Power Sources* 170 (2007) 387.
- [25] J. Kawakita, S. Kuroda, T. Fukushima, H. Katanoda, K. Matsuo, H. Fukanuma, *Surf. Coatings Technol.* 201 (2006) 1250.
- [26] T. Valente, F.P. Galliano, *Surf. Coatings Technol.* 127 (2000) 86.
- [27] H. Ji, P.M. Marquis, *Surf. Coatings Technol.* 45 (1991) 121.
- [28] A.S. Gago, A.S. Ansar, P. Gazdzicki, N. Wagner, J. Arnold, K.A. Friedrich, *ECS Trans.* 64 (2014) 1039.
- [29] W. Yoon, X. Huang, P. Fazzino, K.L. Reifsnider, M.A. Akkaoui, *J. Power Sources* 179 (2008) 265.
- [30] J.F. Moulder, W.F. Stickle, P.E. Sobol, K.D. Bomben, *Handbook of X-Ray Photoelectron Spectroscopy*, Physical Electronics, Inc., Eden Prairie, 1995.

- [31] S.A. Grigoriev, P. Millet, S.A. Volobuev, V.N. Fateev, *Int. J. Hydrogen Energy* 34 (2009) 4968.
- [32] J.W. Schultze, M.M. Lohrengel, *Electrochim. Acta* 45 (2000) 2499.
- [33] O.F. Selamet, M.S. Ergoktas, *J. Power Sources* 281 (2015) 103.
- [34] W.B. Utomo, S.W. Donne, *Electrochim. Acta* 51 (2006) 3338.
- [35] D. Capek, M.P. Gigandet, M. Masmoudi, M. Wery, O. Banakh, *Surf. Coatings Technol.* 202 (2008) 1379.
- [36] Z. Panossian, N.L. de Almeida, R.M.F. de Sousa, G. de Souza Pimenta, L.B.S. Marques, *Corros. Sci.* 58 (2012) 1.
- [37] J.M. Macak, H. Tsuchiya, A. Ghicov, K. Yasuda, R. Hahn, S. Bauer, P. Schmuki, *Curr. Opin. Solid State Mater. Sci.* 11 (2007) 3.
- [38] S.D. James, *J. Electrochem. Soc.* 116 (1969) 1681.
- [39] D.A. Jones, *Principles and Prevention of Corrosion*, 1st Ed., Macmillian, New York, 1992.
- [40] C. Rozain, P. Millet, *Electrochim. Acta* 131 (2014) 160.
- [41] F. Beck, W. Kaiser, H. Krohn, *Electrochim. Acta* 45 (2000) 4691.
- [42] in: Goodfellow, <http://www.goodfellow.com>, accessed September 2014, n.d.
- [43] C.Y. Ho, T.K. Chu, *Electrical Resistivity and Thermal Conductivity of Nine Selected AISI Stainless Steels*, CINDAS Report 45, 1977.
- [44] D.R. Lide, ed., *Handbook of Chemistry and Physics*, Vol. 84, CRC Press, 2003.

## Tables

Table 1. Structural parameters of Pt and Ti in the Pt/Ti and Ti coatings, respectively, calculated using a Rietveld analysis.

Metal	Pt (in Pt/Ti/ss)	Ti (in Ti/ss)
Phase	Platinum	Titanium
Space group	Fm-3m	P63/mmc
Lattice parameters		
a (Å)	3.94146 (10)	2.95359 (19)
c (Å)	-	4.69264(26)
Cell volume (Å <sup>3</sup> )	61.23112 (18)	35.4526 (20)
Crystallite size (nm)	117.7 (36)	30.37(25)
Crystal density (g cm <sup>-3</sup> )	21.1615 (17)	13.45576 (75)

Table 2. Electrochemical parameters including the corrosion potential ( $E_{corr}$ ), corrosion current density ( $j_{corr}$ ), anode ( $\beta_a$ ) and cathode ( $\beta_c$ ) Tafel slopes and polarisation resistance ( $R_p$ ). The iron concentrations ([Fe<sup>2+</sup>]), which were measured at the end of the chronoamperometric test in Figure 7a and Figure S6a (supporting information), are listed in the last column.

Sample	$E_{corr}/V$ vs. RHE		$j_{corr}/\mu A\ cm^{-2}$		$\beta_a/mV\ dec^{-1}$		$\beta_c/mV\ dec^{-1}$		$R_p/x\ 10^3\ \Omega$		[Fe <sup>2+</sup> ]/ppm
	Before	After	Before	After	Before	After	Before	After	Before	After	After
Stainless steel (ss)	0.36	0.54	1.7	0.6	50	56	20	34	3.7	15.3	100.8
Ti/ss	0.22	0.46	0.71	0.44	99	102	92	73	29.2	42.0	0 <sup>1</sup>
Pt/ss	0.91	0.94	1.22	0.66	53	17	19	21	5.0	6.2	27.7
Pt/Ti/ss	0.93	0.92	0.73	0.56	29	13	22	15	7.5	5.4	0 <sup>1</sup>

<sup>1</sup>Below the detection limit of the photometer.

Table 3. Cost and electrical conductivities of potential base materials for BPPs for PEM electrolyser stacks.

Metal	Cost (30 x 30 x 0.3 cm <sup>3</sup> ) in USD [42]	Electrical resistivity (10 <sup>-8</sup> Ω m) at 273 K [43,44]
Titanium (≥ 99.6%)	614	39
Fe/Cr18/Ni10 (ss 304)	268	69.6
Copper (99.9%)	242	1.54
Aluminium (99%)	161	2.42

## Figure captions

Fig. 1. Cross-sectional scheme of a PEM electrolyser anode. The dashed circle indicates the area of contact between the BPP and the current collector (e.g., thin mesh) and the oxygen evolution reaction (OER) catalyst layer. This region is the most prone to degradation due to the acidity of the environment under high potentials.

Fig. 2. Scheme of (a) Pt/Ti and (b) Pt coatings deposited on stainless steel (ss), indicating the zone of the sample that was submitted to corrosion tests, while the rest was protected by a silicone O-ring. Photos of Pt/Ti/ss and Pt/ss after the corrosion tests are shown in (c) and (d), respectively. The corroded and non-corroded areas used for physical analysis are indicated as A and B, respectively.

Fig. 3. Cross-sectional SEM images of the Pt/Ti coatings on stainless steel (a) before and (b) after corrosion measurements; corresponding magnified views of the interface between the Ti and Pt are shown in (c) and (d), respectively. Samples without the Ti layer between the Pt and stainless steel (e) before and (f) after the corrosion test; the corresponding cutaways are presented in (g) and (h), respectively.

Fig. 4. AFM images of Pt/ss before the corrosion tests showing (a) topography and (b) peak force; Pt/Ti/ss before the corrosion test with (c) topography, (d) peak force; and Pt/Ti/ss after the corrosion test showing (e) topography, (f) peak force, and (g) current.

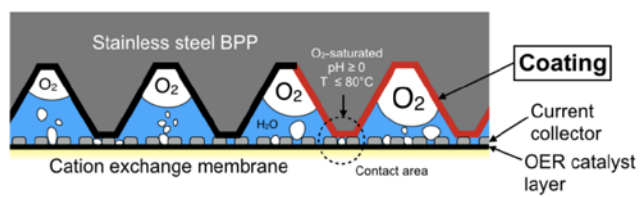
Fig. 5. (a) XRD patterns measured from the top of the Pt/Ti/ss and Ti/ss surfaces. The inset shows a cutaway view of the Pt/Ti/ss spectrum, in which empty and filled symbols correspond to Pt and Ti, respectively. XPS (b) Ti2p and (c) O1s spectra of ion etched Pt/Ti/ss. The spectra of an anodised Ti/ss sample are shown for comparison purposes. (d) Measurements of interfacial contact resistance (ICR) vs. compaction force on the Pt/Ti/ss, Ti/ss and Pt/ss samples as prepared.

Fig. 6. (a) Potentiodynamic characteristics of the Ti/ss sample (16 coating runs), Ti foil and uncoated stainless steel (ss) samples in O<sub>2</sub>-saturated 0.5 M H<sub>2</sub>SO<sub>4</sub> at 65 °C. A second scan for the Ti/ss sample is also included. (b) Potentiodynamic characteristics of Ti/ss (32 coating runs) before and after the anodisation process carried out at  $E_{const} = 2$  V vs. RHE. The scan rate was 1 mV s<sup>-1</sup>. The inset shows the corresponding current transient vs. time. (b) Chronoamperometric characteristics at  $E_{const} = 2$  V vs. RHE of anodised Ti/ss (8 coating runs) and bulk Ti. The inset shows a cross-section SEM image of the Ti/ss sample used in this experiment. Measurements were carried out at in O<sub>2</sub>-saturated 0.5 M H<sub>2</sub>SO<sub>4</sub> at 80 °C.

Fig. 7. (a) Chronoamperometric tests on Pt/Ti/ss, Pt/ss and Ti/ss samples. The Pt-based samples and Ti/ss were polarised to  $E_{const} = 2$  V vs. RHE for 6 h and 16 h, respectively. The inset shows a cutaway view of the current transient of Ti/ss sample. (b) Potentiodynamic characteristics of the Pt/Ti/ss, Pt/ss and Ti/ss samples before and after the corrosion test in (a), carried out at a sweep rate of 1 mV s<sup>-1</sup>. For the sake of clarity only the curves of Ti/ss after the anodisation experiment are shown. The first (s1, dotted line) and fifth (s5, dashed line) linear voltammetric scans of Pt/ss are indicated as well. The rest of the scans are presented in Figure S6b of the supporting information. Measurements were carried at in O<sub>2</sub>-saturated 0.5 M H<sub>2</sub>SO<sub>4</sub> at 80 °C.

Fig. 8. Cell voltage vs. current density characteristics of a PEM electrolyser cell with an anode electrode holder (EH) made of stainless steel and coated with Pt/Ti. Forward and backward scans were performed at 67 and 76 °C, respectively. The left inset shows a photo of the coated EH before assembling the cell. The right inset shows the cell voltage and temperature with respect to time under a constant loading ( $I_{const}$ ) of 1.2 A cm<sup>-2</sup>. All the measurements were carried out at 1 bar.

**Figure 1**



**Figure 2**

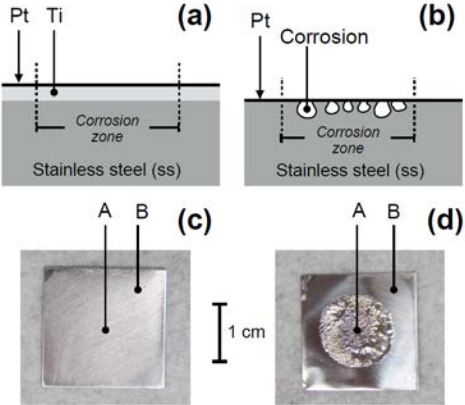


Figure 3

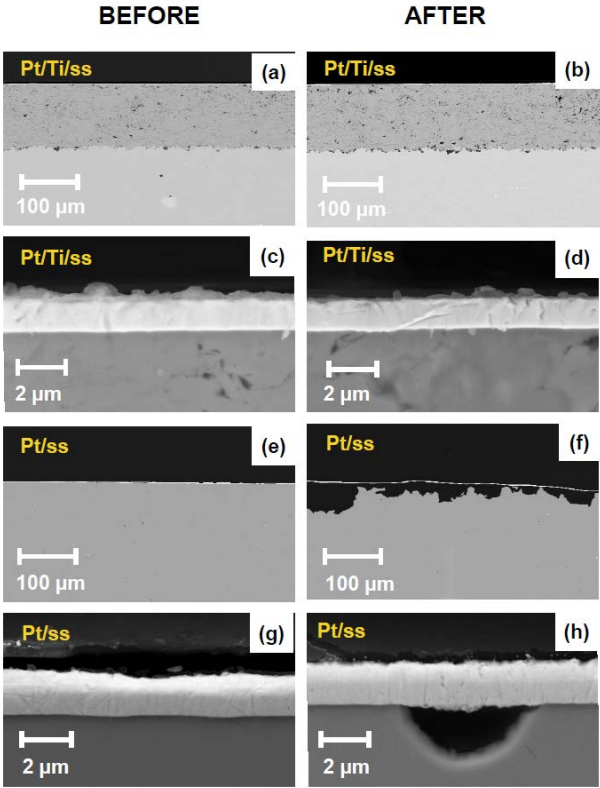
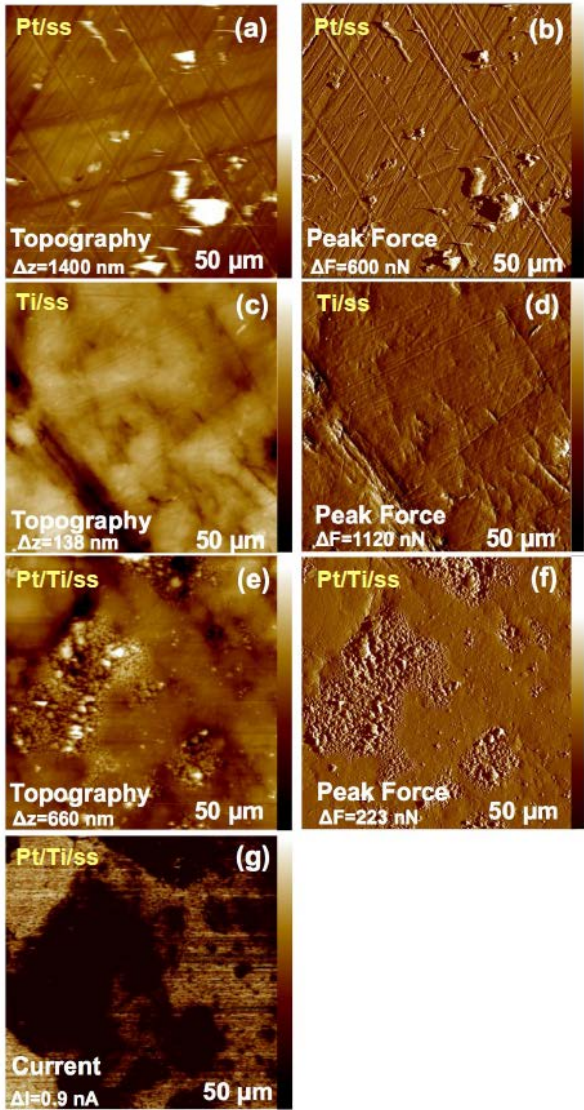


Figure 4



**Figure 5**

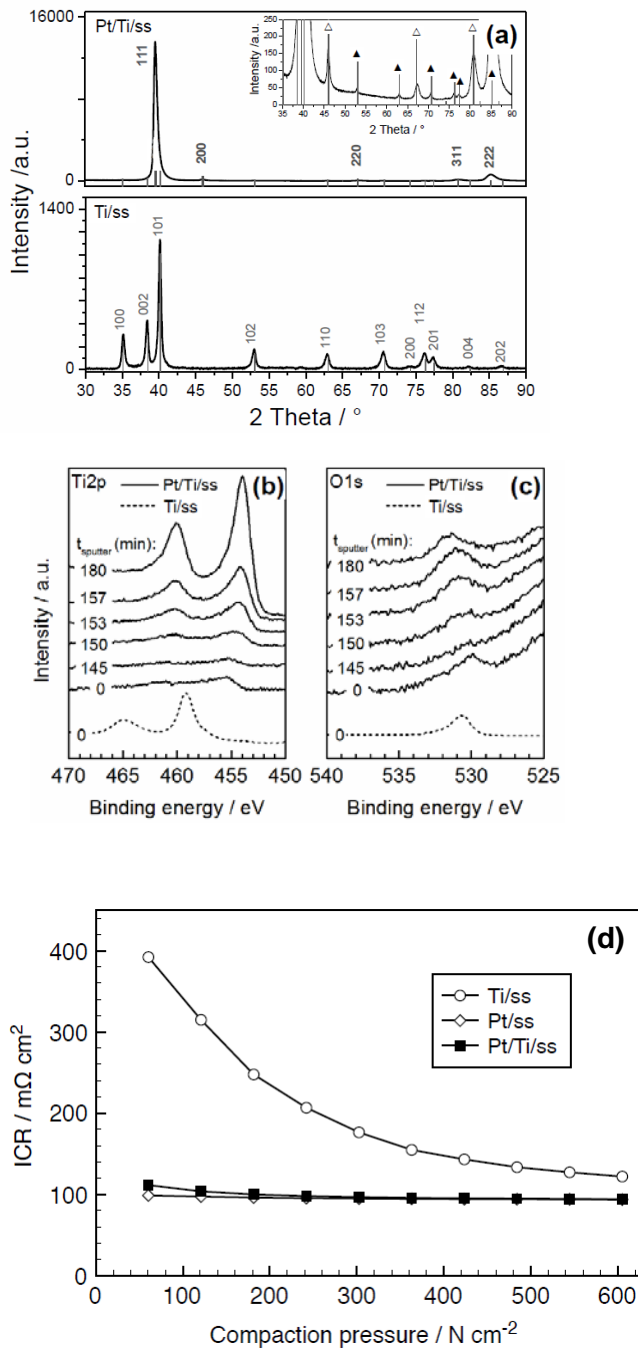


Figure 6

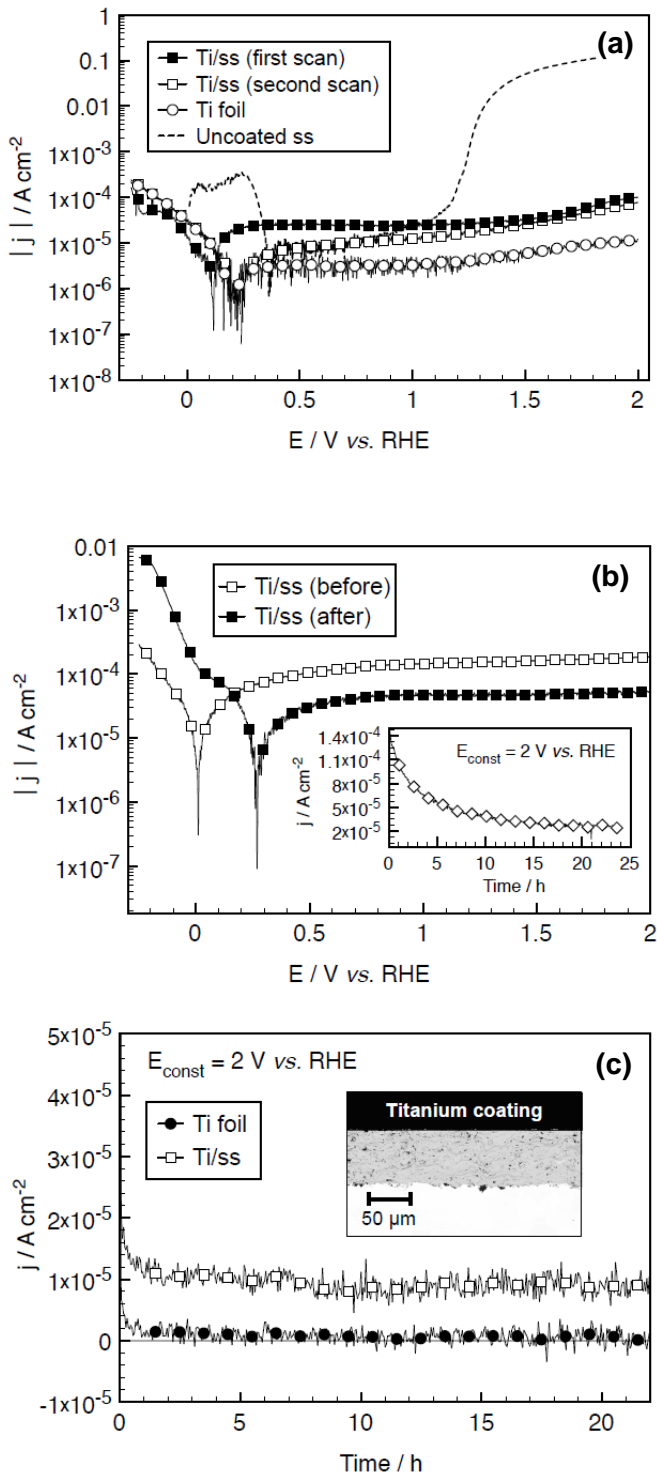


Figure 7

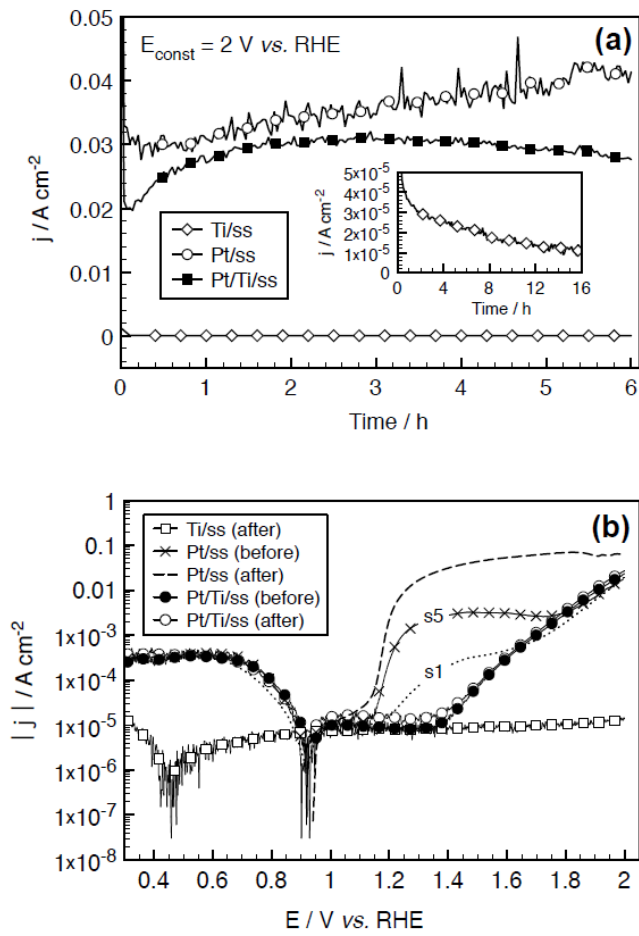
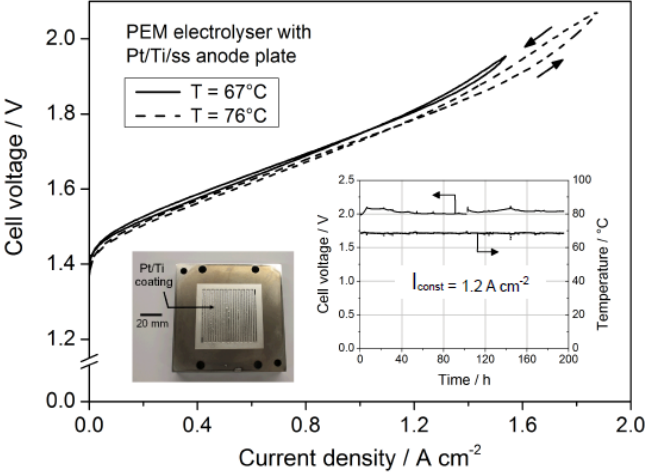


Figure 8



# Supporting information of “Protective coatings on stainless steel bipolar plates for proton exchange membrane (PEM) electrolyzers”

A. S. Gago<sup>1,\*</sup>, S. A. Ansar<sup>1</sup>, B. Saruhan<sup>2</sup>, U. Schulz<sup>2</sup>, P. Lettenmeier<sup>1</sup>, N. A. Cañas<sup>1</sup>, P. Gazdzicki<sup>1</sup>, T. Morawietz<sup>3</sup>, R. Hiesgen<sup>3</sup>, J. Arnold<sup>1</sup>, K. A. Friedrich<sup>1,4</sup>

<sup>1</sup>Institute of Engineering Thermodynamics, German Aerospace Centre, Pfaffenwaldring 38-40, 70569 Stuttgart, Germany

<sup>2</sup>Institute of Materials Research, German Aerospace Centre, Linder Hoehe, 51147, Cologne, Germany

<sup>3</sup>University of Applied Sciences Esslingen, Dept. of Basic Science, Kanalstrasse 33, 73728, Esslingen, Germany

<sup>4</sup>Institute for Energy Storage, University of Stuttgart, Keplerstraße 7, 70550 Stuttgart, Germany

\*e-mail address: aldo.gago@dlr.de (A. S. Gago)

## 1. EDX analysis

Elemental or energy dispersive X-ray analysis (EDX) was carried out on the surface of flat samples of Ti/ss to determine the purity of the coatings. Figure S1a and S1b show an SEM image of the surface of a Ti coating and the corresponding EDX spectrum, respectively. Only the elements Ti (97.04%), C (2.38%), Si (0.52%) and Al (0.07%) were detected. SEM images at higher magnifications (not shown) revealed that small particles of SiC from the sandpaper were encrusted in the protuberances of the Ti coating. However, these particles do not pose an issue as SiC is resistant to corrosion in an acidic environment [1].

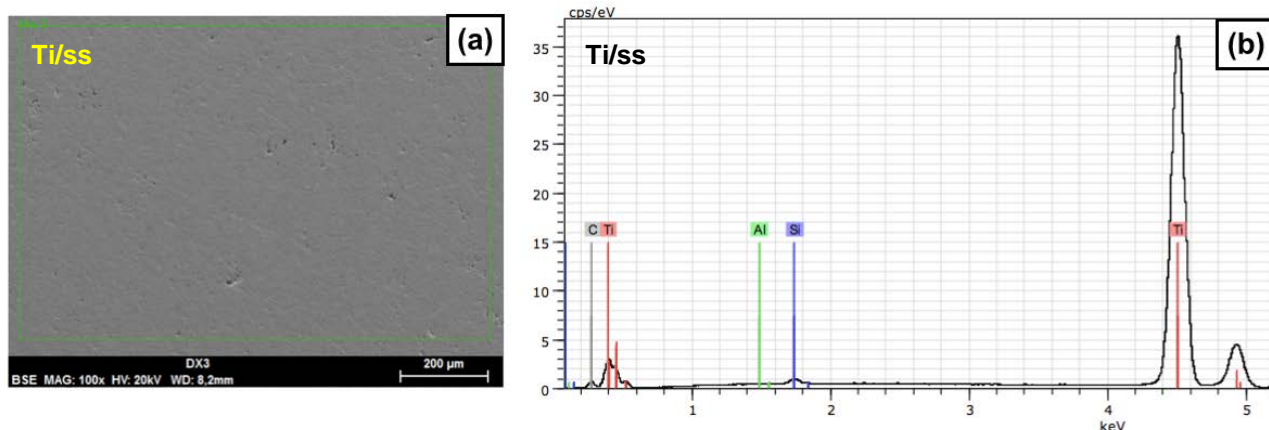


Fig. S1. (a) Topographic SEM image of a Ti/ss coating. (b) EDX spectrum of the area delimited by the green square.

## 2. AFM analysis of the Pt/ss samples

Figure S2a and S2b show the topography and peak force images, respectively, on a Pt/ss sample after corrosion measurements. The corrosion of the stainless steel substrate is evident from the high surface roughness shown in both images. Interestingly, the overall surface is quite homogeneous and the corrosion features have similar sizes. A characteristic region illustrating clearly the acute pitting corrosion is shown in another topographic image, Figure S2c. Figure S2d presents the corresponding adhesion image. Relatively large height differences with areas of high and low

roughness can be observed. Especially illustrative of the two distinctive materials is the mapping of adhesion in Figure S2d. The area of high roughness corresponds to the formerly underlying steel substrate, whereas the smooth areas are associated with the remaining Pt layer.

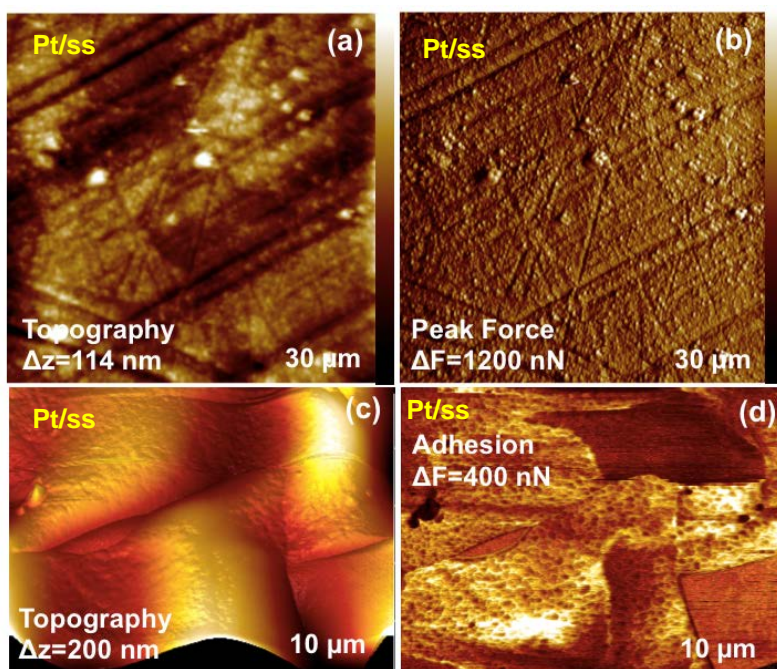


Fig. S2. (a), (c) Topography, (b) peak force and (d) adhesion AFM images of a Pt/ss sample after the electrochemical measurements.

### 3. Rietveld analysis

Figure S3 and Figure S4 show the measured and fitted spectra of the Pt/Ti and Ti coating. Only the fitted spectra of the main phase can be observed. The Rietveld analysis was performed using Topas 4.2 software (Bruker) [2]. The instrumental function was determined using  $\text{Al}_2\text{O}_3$  as a reference. Lattice parameters, scale factors, preferred crystallographic orientations, and microstructural parameters were refined. In particular, Pt/Ti/ss shows a preferential orientation of the crystallites, which can be observed from the high relative intensity of the (111) peak at approximately  $40^\circ$ . For this reason, it was possible to achieve a satisfactory refinement by selecting only two preferred orientations: (111) and (311), in which the fraction for the direction (111) was 0.65 higher than for (311). The weighted-pattern residuals (Rwp) of the refinements were 16.38 and 5.18 for the Pt/Ti and Ti coatings, respectively.

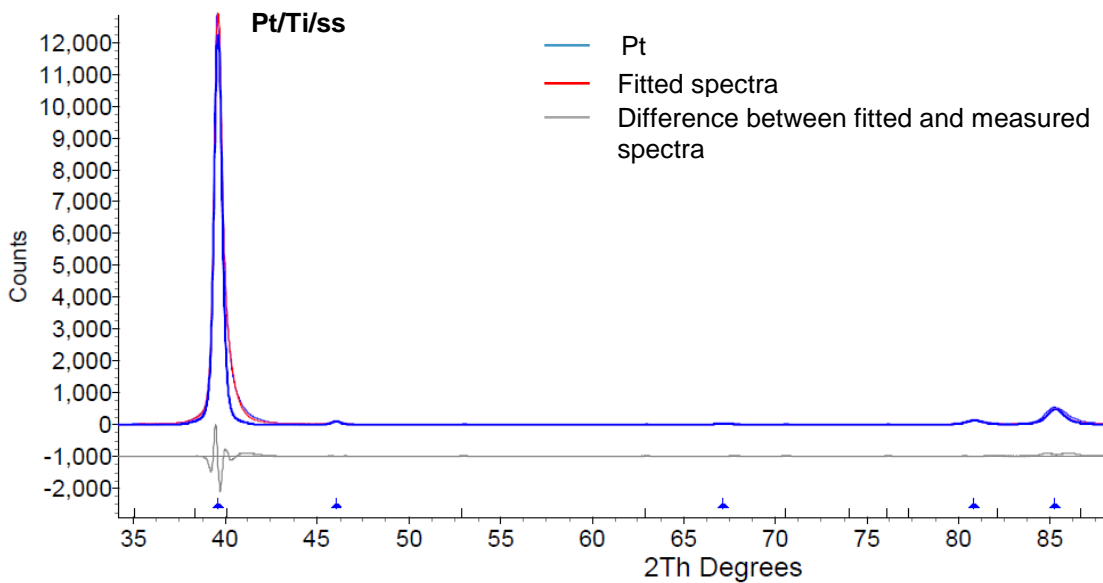


Fig. S3. Rietveld analysis of the Pt/Ti coating. XRD spectrum was fitted with the crystalline phases of Pt (Fm-3m) and Ti (P63/mmc).

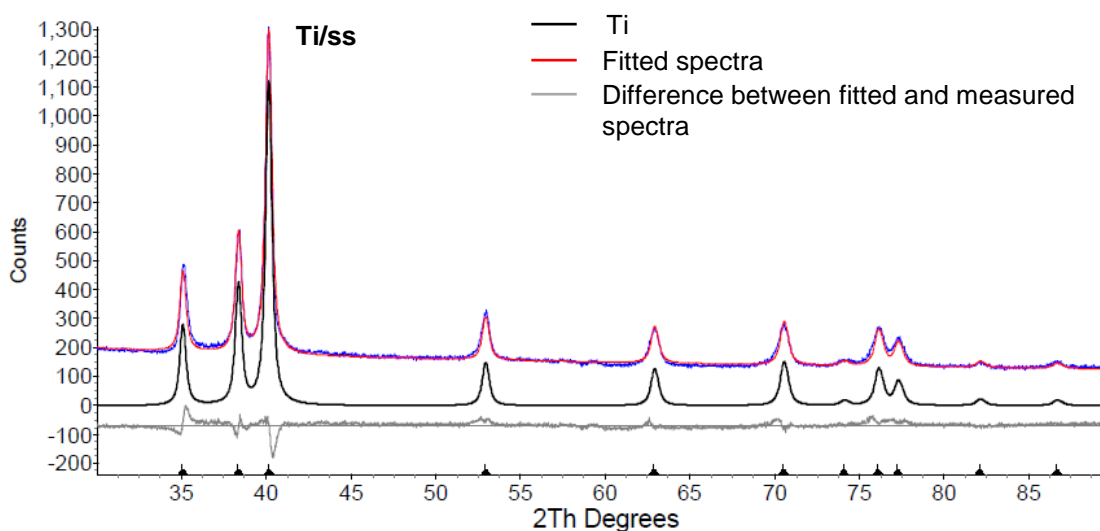


Fig. S4. Rietveld analysis of the Ti coating. XRD spectrum was fitted with the crystalline structure of Ti (P63/mmc).

#### 4. XPS deep profiles

Figure S5a and S5b shows the XPS sputtering deep profiles of Ti/ss and Pt/Ti/ss samples, respectively. Both samples were exposed to air before the sputtering process. Figure S5a shows that the Ti surface is passivated by a mixed phase of  $\text{TiO}_2/\text{Ti}$  or rather an amorphous  $\text{TiO}_2$  phase. Removing the oxide layer takes approximately 250 seconds of sputtering with Ar-ions on the thermally sprayed Ti coating. In the case of the Pt/Ti/ss coating shown in panel (b), removing the Pt layer by sputtering took more than 8000 s. After removing the Pt, the mixed  $\text{TiO}_2/\text{Ti}$  phase could not be detected on the Pt/Ti interface. The absence of  $\text{TiO}_2$  between the Pt and Ti coatings is critical for improving the adherence of Pt to the Ti and for reducing the ICR.

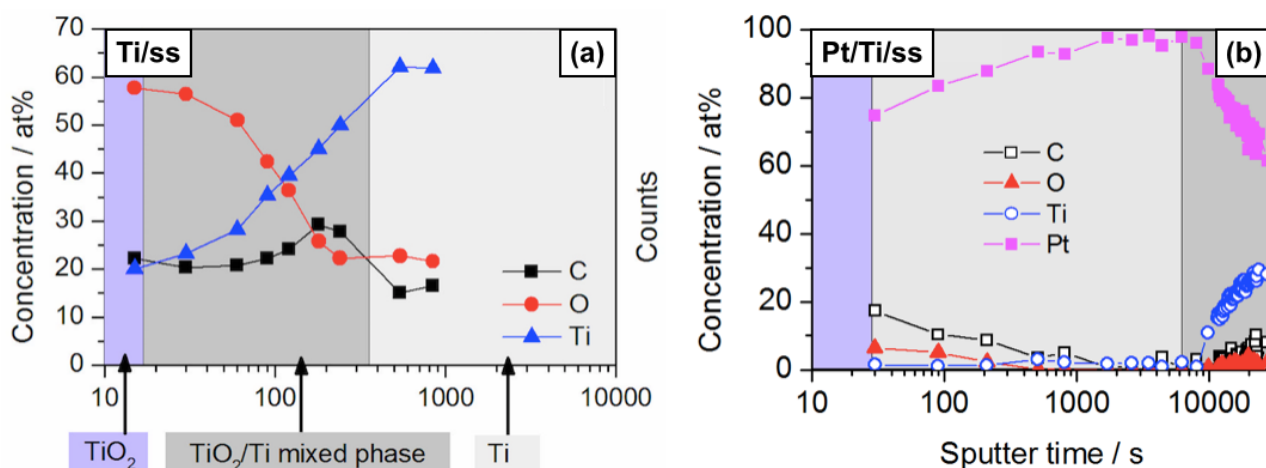


Fig. S5. XPS sputtering deep profiles of (a) Ti/ss and (b) Pt/Ti/ss samples.

## 5. Corrosion measurements

Figure S6a shows the chronoamperometric characteristics of an uncoated sample, carried out at  $E_{const} = 1.5 \text{ V vs. RHE}$  in  $\text{O}_2$ -saturated  $\text{H}_2\text{SO}_4$  at  $65 \text{ }^\circ\text{C}$ . The experiment could not be performed at  $E_{const} = 2 \text{ V vs. RHE}$  like the rest of the electrochemical measurements as the measured current was already over the reading limit of the potentiostat. The experiment was stopped after 1 h and reinitiated again afterwards. After two hours, the electrolyte was heavily polluted with  $\text{Fe}^{2+}$  and  $\text{Cr}^{3+}$ , giving it a yellowish colour (see photo in Figure S6a). Therefore, further testing of uncoated stainless steel was out of the scope of this work.

Figure S6b is an enlarged cutaway view section of Figure 7b in the main text between  $1 \text{ V}$  and  $1.9 \text{ V vs. RHE}$ , including the five linear voltammetric scans that were performed on the Pt/ss sample prior to the chronoamperometric test. This figure shows how the electrolyte was gradually accessing the stainless steel substrate, which resulted in pitting corrosion during each scan. The threshold potential is ca.  $1.15 \text{ V vs. RHE}$ , at which  $\text{Fe}^{2+}$  starts oxidising to  $\text{Fe}^{3+}$ . At the end of the chronoamperometric test, a sharp increase in the current density was measured, which also occurred case for an uncoated sample. In contrast, the Pt/Ti/ss sample did not show any increase in the current density before  $1.4 \text{ V vs. RHE}$ , either before or after the chronoamperometric measurements.

Fig. S6. (a) Chronoamperometric test on uncoated stainless steel (ss) substrate, carried out at  $E_{const} = 1.5 \text{ V vs. RHE}$  in  $\text{O}_2$ -saturated  $\text{H}_2\text{SO}_4$  at  $65 \text{ }^\circ\text{C}$ . A photo of the electrode holder immersed in the electrolyte is shown in the inset. (b) Potentiodynamic characteristics of the Pt/Ti/ss and Pt/ss before and after a chronoamperometric test at  $E_{const} = 2 \text{ V vs. RHE}$ , performed in  $\text{O}_2$ -saturated  $\text{H}_2\text{SO}_4$  at  $65 \text{ }^\circ\text{C}$  at a sweep rate of  $1 \text{ mV s}^{-1}$ . Scans 1 (s1) to 5 (s5) of Pt/ss before the chronoamperometry are also indicated.

## 6. Cost of Ti coating for industrial scale

The vacuum chamber of the thermal spraying facility at the DLR is fitted with a hexagonal turn table that is capable of holding 6  $2500 \text{ cm}^2$  plates and performing 4 runs per day. Therefore, an area of  $60,000 \text{ cm}^2$  can be sprayed with Ti in 8 hours by a batch-process vacuum plasma spraying (VPS). In low-volume batch production, some of the major expenses arise from idle time during which no spraying is performed, including substrate heating cooling in chamber, vacuuming and de-vacuuming the large vessel. In large volume production, coating costs can be reduced significantly by depositing the part to be coated in continuous-processing equipment consisting of a substrate exchanger, heater and a vacuum plasma coating chamber. A stack of stainless steel substrates would be introduced into the equipment and heated up prior to the coating of each substrate. Using a defined set of process parameters and double powder injection, it would take ca. 64 seconds to

produce a 120  $\mu\text{m}$  thick Ti coating on a 1000  $\text{cm}^2$  area, leading to a throughput of 56 substrates per hour using equipment with one plasma gun. Considering a production unit with three automated spray guns and support robots for handling the substrates in one chamber, overseen by one trained technician, the cost of vacuum coating stainless steel bipolar plates with Ti can be estimated as follows:

Total throughput per hour: 168 pieces

Labour cost per hour: 66 €

Equipment cost per hour: 96 €(working in 2 8-hour shifts per day, 5 days per week)

Ti powder per piece: 1.44 €(powder price 40,000 €per MT)

Other consumables (gases, electricity, etc.) per piece: 0.31 €

Net cost per 1000  $\text{cm}^2$  bipolar plate = 2.91 €per piece = 3.13 USD or 30.8 USD per square metre of bipolar plate (March 2014)

Labour and equipment costs per hour were taken from the current salary of a technician and the actual market price which DLR offers for the use of its plasma spraying facility.

## References

- [1] P. Misaelides, F. Noli, J.P. Riviere, J. Delafond, Nucl. Instruments Methods Phys. Res. Sect. B Beam Interact. with Mater. Atoms 129 (1997) 221.
- [2] T.V.. Bruker AXS, Karlsruhe, General Profile and Structure Analysis Software for Powder Diffraction Data, Users's Manual, 2009.